1   **Supporting Information of "Deciphering electrochemical**

2   **interactions in metal-polymer catalysts for CO₂ reduction"**

3

4 Xingyu Wang[1], Sanjubala Sahoo[2,3], Jose Gascon[4], Mikhail Bragin[5], Fangyuan Liu[2], Julia

5 Olchowski[1], Samuel Rothfarb[1], Yuankai Huang[1], Wenjun Xiang[1], Pu-Xian Gao[2,3], S. Pamir

6 Alpay[2,3], Baikun Li[1*]

7

8 [1]Department of Civil and Environmental Engineering, University of Connecticut, Storrs,

9 Connecticut 06269-3037, USA

10 [2]Institute of Materials Science, University of Connecticut, Storrs, Connecticut 06269-3136, USA

11 [3]Department of Materials Science and Engineering, University of Connecticut, Storrs,

12 Connecticut 06269-3136, USA

13 [4]Department of Chemistry, University of Connecticut, Storrs, Connecticut 06269-3037, USA

14 [5]Department of Electrical and Computer Engineering, University of Connecticut, Storrs,

15 Connecticut 06269-3037, USA

16

17

18

19

Theory S1. Theory of Multiscale Model

S1.1 Transport and distribution model (system level).

The system level implements the transport of molecules in the catholyte and the cathode surface. To well correspond with our experimental evaluation, the catholyte is set to be 0.1M of $KHCO_3$ solution in the multiscale model development, and all the molecular distribution and pH (6.8 with saturated CO_2) are assumed to be even and homogenous in the bulk phase under the mixing effect due to the continuous sparging of CO_2, meaning that the only diffusion resistance comes from the heterogenous cathode-bulk boundary layer ($10\ \mu m$). As the concentration of catholyte is considered dilute, Poisson-Nernst-Plank (PNP) equation achieved by coupling Nernst-Planck equation (Eq.1) and Poisson equation (Eq.2) together, is used for the profiling of bulk solution mass conservations[1]:

$$\frac{\partial c_i}{\partial t} = \nabla \cdot D_i \left(\nabla c_i + \frac{z_i c_i \nabla \phi}{k_B T} \right) \qquad \text{(Eq.1)}$$

$$-\nabla(\epsilon_w \epsilon_0 \nabla \phi) - \lambda \sum_i z_i c_i = Q \qquad \text{(Eq.2)}$$

In which c_i and z_i are the concentration and charge of molecules in the solution. Here we consider the existence of CO_2, H^+, OH^-, K^+/Na^+, HCO_3^-, and CO_3^{2-} in the electrolyte. The boundary conditions for c_i and z_i in Nernst-Planck equation and Poisson Equation have been defined in Table S7. D_i represents diffusion coefficients o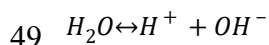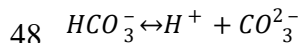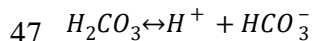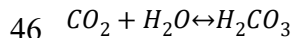f molecules, which can be found in Table S8. k_B and T are Boltzmann constant and temperature ($20\ °C$ or 293K), respectively. ϕ is the electrostatic potential. ϵ_w and ϵ_0 represent the dielectric permittivity water and vacuum. Q is the permanent charge density, which is calculated through Eq.3[2]:

$$Q(x) = \sum_i z_i \delta(x - x_i) \qquad \text{(Eq.3)}$$

41 Where x represents the position/distance from the cathode surface and the δ is the δ-function for

42 discrete charge calculation. The existence of homogenous buffer reaction (CO_2 hydration and acid-

43 base equilibrium) due to the coexistence of CO_2, H^+, OH^-, HCO_3^-, and CO_3^{2-} associated pH with the

44 concentration of CO_2, where the correlation has been summarized below (in the form of H^+

45 association/dessociation):

46 $CO_2 + H_2O \leftrightarrow H_2CO_3$

47 $H_2CO_3 \leftrightarrow H^+ + HCO_3^-$

48 $HCO_3^- \leftrightarrow H^+ + CO_3^{2-}$

49 $H_2O \leftrightarrow H^+ + OH^-$

50 For the solution close to the cathode surface, as there is no obvious concentration divergence

51 beyond 5nm from the cathode surface, we determine that the Helmholtz layer of the continuum

52 model mainly exists in this region (Figure 1). The aggregation effect of cations leads to a different

53 transport phenomenon compared to the diluted bulk solution. Because the PNP equation might fail

54 within the CO_2RR onset range in our study (absolute value: $\sim 0.4V - 1.5V\ vs\ RHE$), which is above

55 the thermal potential ($\frac{k_B T}{e} = 25mV$)[3], Stefan-Maxwell equation is applied (Eq.4) in the hydraulic

56 boundary near the cathode surface[4]:

57 $$\nabla \ln a_i = \sum_i \frac{c_i}{cD_{ij}}\left(\frac{J_j}{c_j} - \frac{J_i}{c_i}\right) \qquad\qquad\qquad \text{(Eq.4)}$$

58 Where a_i and J_i is the activity and flux of molecules. c is the total molar concentration. D_{ij} is Stefan-

59 Maxwell diffusion coefficient, which is calculated through Darken equation (Eq.5)[5]:

60 $$D_{ij} = c_i D_j + c_j D_i \qquad\qquad\qquad \text{(Eq.5)}$$

61 In the Helmholtz layer area, CO_2 tends to be absorbed onto the cathode surface, where the

62 adsorption energy can be described through thermodynamic model (Eq.6)[6]:

3

63 $$\Delta G_{CO_2} = -RT\ln\left[\frac{K_L}{\gamma}\right]$$ (Eq.6)

64 where K_L, γ are Langmuir equilibrium constant and activity coefficient.

65 **S1.2 Electrochemistry model (molecular level).**

66 The molecular level of electrochemistry describes the reduction kinetics and losses contributed by

67 the mass transport and charge transfer. As the kinetics of the cathode is described through

68 microkinetic models, for the anode surface, only oxygen evolution reaction (OER) is expected to

69 happen, which can be described by Tafel kinetics (Eq.7)[7]:

70 $$j_a = j_{0a} \cdot e^{\frac{2\alpha_a F\eta}{RT}}$$ (Eq.7)

71 Where the j_0 and α was set to be $4.684 \times 10^{-9}\, mA/cm^2$ and 0.5 respectively[8].

72 The cathodic kinetics is determined through microkinetic model. The reaction rates of elementary

73 steps in the Mechanism I and Mechanism II are calculated through the power-law of rate equation

74 separately (Theory S2), where the rate constant is determined through transition state theory

75 (Eq.8)[9]:

76 $$k_i = \frac{k_B T}{h} c_i \cdot e^{\left(-\frac{\Delta G}{k_B T}\right)}$$ (Eq.8)

77 In which k_i is the rate constant and h is the Planck number. ΔG represents the activation free energy

78 for the ith reaction, which is calculated through the quantum chemistry model (the atomistic level)

79 using VASP. c_i here represents the concentration in the Helmholtz layer near the cathode surface,

80 which is different from bulk concentration and is determined in the transport and distribution

81 model (the system level). In the microkinetic model, the power rate law associated with transition

82 state theory shifts from quasi-monomolecular surface adsorption kinetics for Eley-Rideal (ER)

83   mechanism (Eq.9) towards bimolecular surface adsorption kinetics for Langmuir-Hinshelwood

84   (LH) mechanism (Eq.10):

85 $$r = k_1 c_{*CO_2} \theta_{*H^+} \qquad \text{(Eq. 9)}$$

86 $$r = k_2 \theta_{*CO_2} \theta_{*H^+} \qquad \text{(Eq. 10)}$$

87   where k is the rate constant calculated from transition state theory, θ_{*CO_2} and θ_{*H^+} represents the

88   adsorbed CO_2 and H^+ on the cathode surface, and $c_{CO_2^+}$ is the H^+ concentration in Helmholtz layer.

89   The major difference of ER (Eq.9) and LH (Eq.10) is reflected on the CO_2 representation from

90   unabsorbed form (c_{*CO_2}) to absorbed form (θ_{*CO_2}), as well as the change of kinetic constant k.

91   The effect of $Cu - Cation - CO_2$ triple binder electron bridge is considered by introducing a cation

92   coverage factor $\theta_{*Cation}$ to explicate the change of reaction rate. $\theta_{*Cation}$ is set to be consistent with

93   the cation-Cu ratio in VASP calculation.

94   With the cathodic current density acquired experimentally, the incorporation of experimental

95   current density into the molecular level delivers quantitative coefficients of thermodynamic charge

96   transfer during CO_2RR. Therefore, we can deduce the charge transfer coefficient on cathode as

97   Eq.11:

98 $$\alpha_c = -\frac{RT}{zF\eta} \log \left(j_e - j_a \right) \qquad \text{(Eq.11)}$$

99   Where j_e is the cathodic exchange current density and can be acquired using the microkinetic

100   model (Eq.12)[9]:

101 $$j_e = F k_i (c_{ox}^{1-\beta} c_{re}^{\beta}) \qquad \text{(Eq.12)}$$

102   Where c_{ox} and c_{re} represents the redox pair in each elementary step described in Theory S2. β is

103   the symmetry factor, which can be assumed with free energy barrier (ΔG^*) and the reaction free

104   energy (ΔG) from Vienna ab initio Simulation Package (VASP) (Eq.13)[10]:

105 $$\beta = \frac{\Delta G^*}{\Delta G}$$ (Eq.13)

106 At the heterogenous interface of cathode and catholyte, impedances always exist due to the

107 mass/charge transfer. Moreover, the separation of charges caused by the alternation of the ion

108 distribution in the Helmholtz layer also contributes to the impedance. The charge distribution on

109 the cathode surface on the electrode side represents the charge contributed by the applied potential

110 (Eq.14)[11]:

111 $$\rho_{surf} = \frac{\epsilon_w \epsilon_0 \phi}{xS}$$ (Eq.14)

112 The xS represents the distance of the inner Helmholtz layer. The cumulation of ions on the solution

113 side near cathode surface boosts ionic charge density (Eq.15)[12]:

114 $$\rho_{ion} = \sum_i n_i z_i e_0 \cdot e^{\left(\frac{z_i F \phi}{RT}\right)}$$ (Eq.15)

115 n_i is the molar quantity of the molecule and e_0 is the elementary charge ($1.602 \times 10^{-19} C$). The

116 separation of charge results in a barrier for the mass and charge transport, which is quantified

117 through mass transport loss (Eq.16) and ohmic resistance (Eq.17), respectively[13,14]:

118 $$\eta_{mass} = \frac{RT}{zF} \cdot \ln \frac{j_L}{j_L - j}$$ (Eq.16)

119 $$R_{electrode} + R_{electrolyte} = \frac{\phi}{j}$$ (Eq.17)

120 j_L is the maximum current density where all the CO_2 molecules are consumed. Here we assume

121 this number to be 10 mA/cm^2 from the average value of current density tests. The pristine Cu

122 electrode resistance $R_{electrode}$ is determined through the EIS test to be 10.4 Ω/cm^2.

123 At the initiation stage of the reaction, the partial voltage to overcome the activation energy of the

124 reduction reaction can be quantified through the activation loss (Eq.18)[15]:

$$\eta_{act} = \frac{RT}{\alpha_c F} \ln \frac{j}{j_e}$$

125   (Eq.18)

126   Moreover, the continuous consumption of CO_2 and H^+ contributes to a reversible drop of cathodic

127   potential, which can be quantified as Nernstian loss (Eq.19)[16]:

$$\eta_{Nernstian} = \frac{RT}{F} \ln \left(\frac{c_{H^+ - bulk}}{c_{H^+ - cathode}} \right) + \frac{RT}{zF} \ln \left(\frac{c_{CO_2 - bulk}}{c_{CO_2 - cathode}} \right)$$

128   (Eq.19)

129   The correlations of the major equations above were ascribed in Figure S25.

130   **S1.3 Quantum chemistry (the atomistic level)**.

131   The simulation of the atomistic level is delivered through the density functional theory (DFT)

132   using Vienna ab initio Simulation Package (VASP). First-principles based studies are performed

133   within generalized gradient approximation (GGA) parameterized by Perdew-Burke-Ernzerhof

134   (PBE) for the exchange and correlation functional[17]. As a catalyst system, the Cu surface is

135   considered to investigate the CO_2 reduction mechanism. The (111) surface of Cu is considered due

136   to its high stability compared to other Cu surfaces[18]. The surface is constructed from the bulk FCC

137   crystal structure with equilibrium lattice parameters a = 3.64 Å which is in good agreement with

138   experimental values (3.61 Å). The surface consists of (3✕4) supercells of bulk FCC Cu lattice.

139   Periodic boundary conditions are applied along the surface plane with a simulation box (13.37 ✕

140   10.29 ✕ 22.31) Å3 where a 16 Å vacuum is kept along the z-direction. The top two layers of the

141   Cu(111) surface are allowed to relax while the rest atoms are fixed to constrain to bulk bond

142   lengths.

143   The adsorption energy (Eads) of the molecules on Cu(111) is calculated as

144   $E_{ads}(eV) = E[molecule@Cu(111)] - E[Cu(111)] - E(molecule)$ (Eq.20)

145 where, the first, second, and third terms on the right hand side represent the total energies of

146 molecule@Cu(111) complex, the Cu(111) support, and the various single molecules, respectively.

147 The reaction pathway for the CO_2 reduction mechanisms is studied using the constrained energy

148 minimization method, where a series of images are created between the reactant and the product

149 to investigate the reaction pathway.

150 The effect of PTFE is demonstrated where a monomer (TFE) of PTFE is introduced in the vicinity

151 of the co-adsorbed reactant (CO_2) and reaction intermediates such as COOH, HCOO, CH_2O, CHO

152 and CH_4. The adsorption energy of the respective molecules with PTFE is defined as;

153 $E_{ads} (eV) = E[molecule@Cu(111)@TFE] – E[Cu(111)@TFE] – E(molecule)$ (Eq.21)

154 where, the first, second and the third terms indicate the total energies of the Cu+TFE+molecule

155 complex, polymer-Cu complex and the molecules (e.g., CO_2, COOH, HCOO, CH_2O, CHO and

156 CH_4), respectively.

157 One of the key quantities that drives the reaction kinetics is the energy barrier (EB) which is

158 defined as the total energy difference between the transition state geometry and the reactant.

159 $EB = E_{TS} – E_{Reactant}$ (Eq.22)

160 where the E_{TS} and $E_{Reactant}$ are the total energies of the transition state structure and the reactant,

161 respectively.

162 The orbital-projected spin-polarized density of states (DOS) is calculated using Gaussian smearing

163 with a broadening parameter value 0.05 eV. A cut-off energy of 300 eV is used for clean Cu(111)

164 while for the adsorbed the adsorbed systems, a value of 400 eV is used. Using different energy

165 cut-off energy values for the plane wave expansion of wave function does not change the DOS

166 significantly. The Fermi level remains the same. A same k-mesh (3×3×1) and same exchange-

167 correlation functionals (GGA-PBE) for the geometry optimization are used for the DOS

168 calculations.

169 All computations are carried out using the Vienna *ab initio* Simulation Package (VASP) with the

170 plane wave basis set[19]. The projector-augmented wave method is used for the electron-core

171 interactions[20]. The energy cut-off for the plane waves is taken as 400 eV. The Brillouin zone

172 integrations are done with (3×3×1) k-points mesh. The total energy convergence criteria for

173 geometry optimization are fixed to 10^{-6} eV. The partial charge analysis on each atomic species is

174 done by using the Bader charge method[21].

175 For the free energy change profiles of proton-electron coupled reduction process, as well as the

176 activation energy used in transition state theory, the computational hydrogen electrode (CHE) is

177 implemented in this study (Eq.23)[22]:

178 $$\Delta G = E(Product) - E(Reactant) - \left[\frac{1}{2}E(H_2) - eU - 0.059 \times pH\right] \quad \text{(Eq.23)}$$

179 Where μ represents free energy of reactants/intermediates/products. All those energies have been

180 calculated from VASP as described above. The pH is selected to be 6.8, which is consistent with

181 our experimental setups.

182 **S1.4 Adjustment of model parameter with existence of polytetrafluoroethylene (PTFE)**.

183 The adjustment of surface affinity and polarity is executed by modifying the Cu catalyst with

184 polytetrafluoroethylene (PTFE) that renders binding property of the electrode and carries spatial

185 affinity towards non-charged CO_2[23,24]. Consistently, in the multi-scale model settings, PTFE with

186 exceptionally low dipole moment possesses a relative permittivity (ε) of 2.1 due to the low electric

187 polarizability of fluorine compared to water of 80. Given the paltry wettability of PTFE in the

188 water phase, here we assume there is only one layer of water molecules in the inner Helmholtz

189 Layer and the polarity and surface capacitance of the PTFE-Cu cathode is around 40 times lower

190 than the pristine Cu cathode. In addition, the SEM imaging and EDAX composition analysis

191 indicate that the surface coverage of Cu alters with different ratios of PTFE additives. With a thin

192 layer of the PTFE-Cu mixture catalyst (<10 μm, Figure 2b) casted directly on the surface of carbon

193 cathode, the diffusion of species is only considered in one dimension (Figure 1b). At such a short

194 distance, the difference between the diffusions across PTFE and Cu is trivial, and thus we ignore

195 the possible path in the PTFE structure and assume that PTFE-Cu cathode has the same surface,

196 and the diffusion coefficients (Table S8) are shared for the species diffusion in both Cu and PTFE.

197

198

199 **Theory S2. Elementary steps of CO$_2$RR according to numbers of electron transfer.**

200 Cathode (CO$_2$RR-CO Generation):

201 $^*CO_2 + {^*H^+} + e^- \leftrightarrow {^{**}COOH}$ (1st electron transfer, R1)

202 $^{**}COOH + e^- \leftrightarrow {^*CO} + {^*} + OH^-(aq)$ (2nd electron transfer, R2)

203 Cathode (CO$_2$RR-CH4 Generation *Mechanism I*):

204 *Note: first step from ^{CO_2} to CO was same as above*

205 $^*CO + {^*H^+} + 3{^*} + 2e^- \leftrightarrow {^{****}C} + OH^-(aq)$ (1st & 2nd electron transfer, M1R1)

206 $^{****}C + {^*H^+} + e^- \leftrightarrow {^{***}CH} + 2{^*}$ (3rd electron transfer, M1R2)

207 $^{***}CH + {^*H^+} + e^- \leftrightarrow {^{**}CH_2} + 2{^*}$ (4th electron transfer, M1R3)

208 $^{**}CH_2 + {^*H^+} + e^- \leftrightarrow {^*CH_3} + 2{^*}$ (5th electron transfer, M1R4)

209 $^*CH_3 + {^*H^+} + e^- \leftrightarrow CH_4(g) + 2{^*}$ (6th electron transfer, M1R5)
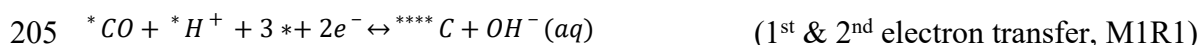
210 Cathode (CO$_2$RR-CH4 Generation *Mechanism II*):

211 *Note: first step from ^{CO_2} to CO was same as above*

212 $^*CO + {^*H^+} + e^- \leftrightarrow {^{**}HCO}$ (1st electron transfer, M2R1)

213 $^{**}HCO + {^*H^+} + e^- \leftrightarrow {^{***}H_2CO}$ (2nd electron transfer, M2R2)

214 $^{***}H_2CO + {^*H^+} + e^- \leftrightarrow {^{***}H_3CO}$ (3rd electron transfer, M2R3)

215 $^{***}H_3CO + {^*H^+} + e^- \leftrightarrow H_4C \cdots {^{**}O} + 2{^*}$ (4th electron transfer, M2R4)

216 $H_4C \cdots {^{**}O} + {^*H^+} + 2e^- \leftrightarrow H_4C \cdots {^{**}OH} + 2{^*}$ (5th electron transfer, M2R5)
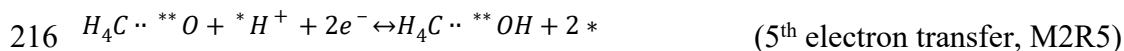
217

218

	Structure-Process-Principle Multiscale Paradigm	Quantum/Molecular Dynamics Simulation	Macro Continuum Simulation	Structure-Principle Limited Multiscale
Transport & Distribution of Molecules & Ions (1st Level)	✓	✗	✓	✓
Electrochemical Kinetics of Reaction (2nd Level)	✓	✗	✓	✓
Surface Process Identification (2nd Level)	✓	✗	✗	✗
Model-Experiment Integration (2nd Level)	✓	✗	✗	✗
Quantum Mechanical Molecular Structure (3rd Level)	✓	✓	✗	✓
Free Energy & Barrier Energy Profile (3rd Level)	✓	✓	✗	✓

Figure S1. Comparison of the multiscale model in this study with other methods[3,25–31].

Compared to previously reported multiscale studies, our method outperforms conventional models that are based solely on molecular structures and enabled discovery of the deterministic role of the surface reaction processes. Our molecular level functions as a bridge connecting the continuum model (system level) and quantum/atomistic model (atomistic level) using an electrochemical spectrum model. Verifying the multiscale model through experiments further improves the integrity of our study.
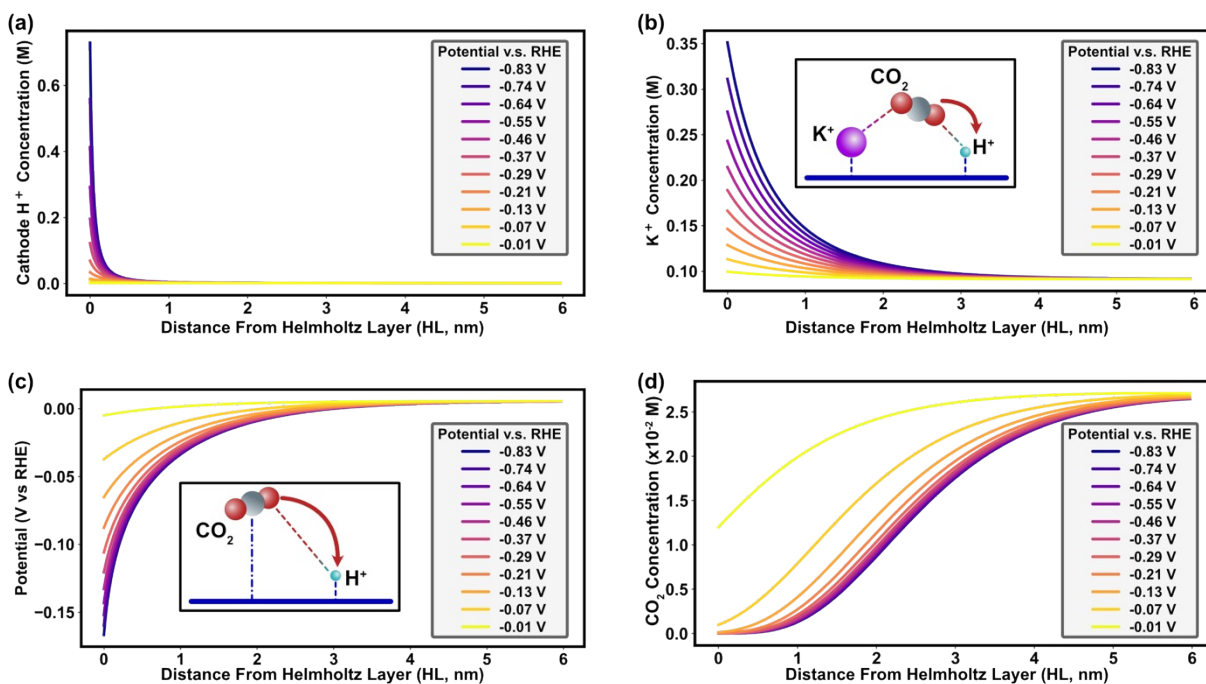
Figure S2. (a) Cathodic potential drop outside the Helmholtz layer; (b) Cathodic K^+ concentration outside the Helmholtz layer; (c) Cathodic H^+ concentration outside the Helmholtz layer ; and (d) Cathodic CO_2 concentration outside the Helmholtz layer.
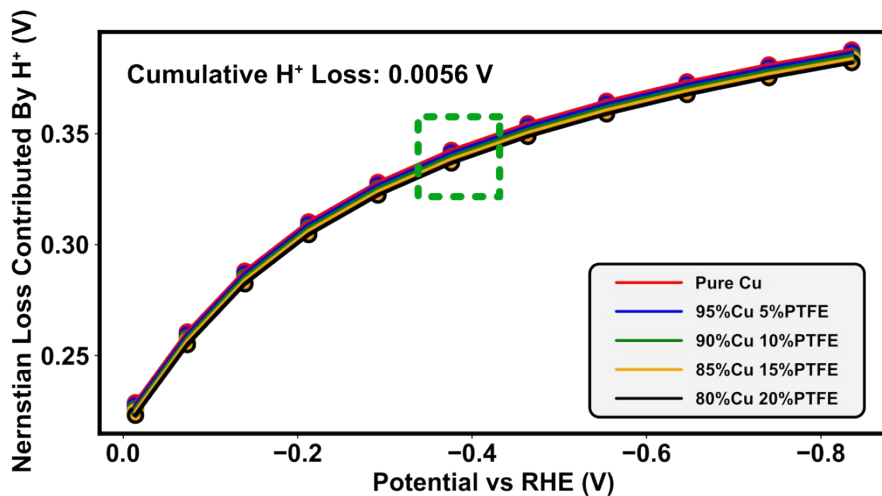
(a)

(b)
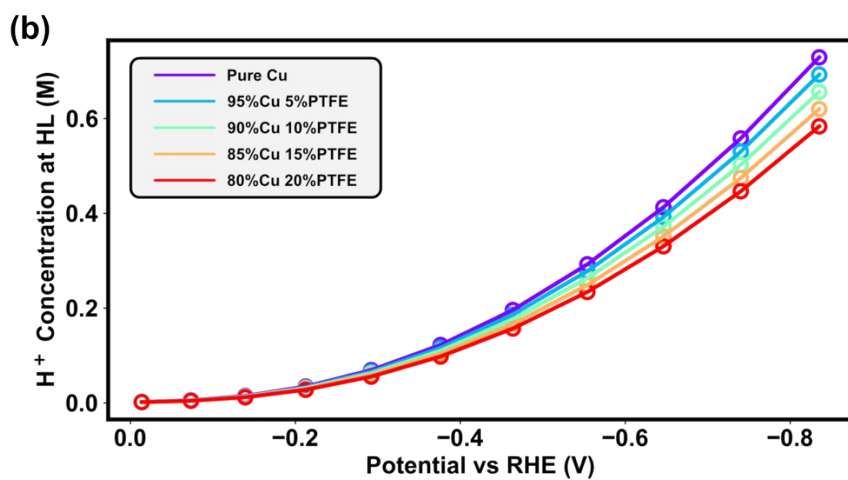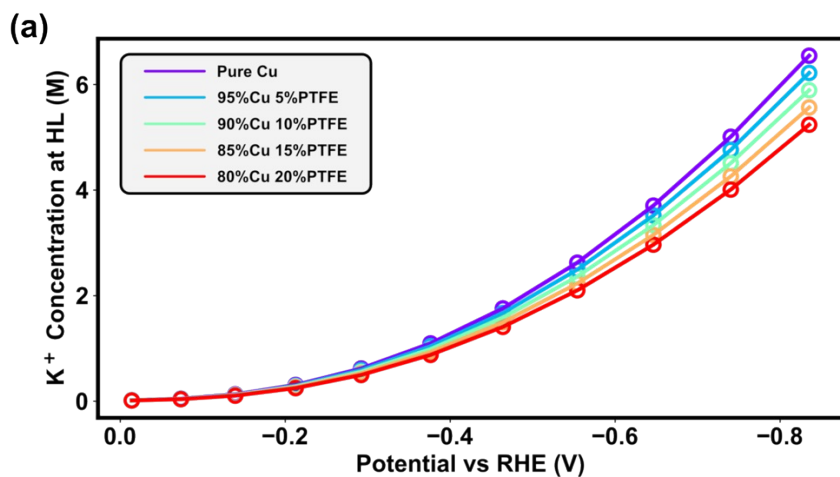
234

235

236 **Figure S3.** (a) Variation of K^+ concentration with potential on the Cu cathodes at different PTFE

237 ratios from 0% to 20%; (b) Variation of H^+ concentration with potential on the Cu cathodes at

238 different PTFE ratios from 0% to 20%.

239

240

Figure S4. Variation of Nernstian loss contributed by H$^+$ with potential on the Cu cathodes at different PTFE ratios from 0% to 20%.

Criteria for Molecular Reactivity: Sabatier Principle (Quantified By Binding Energy of Molecules)
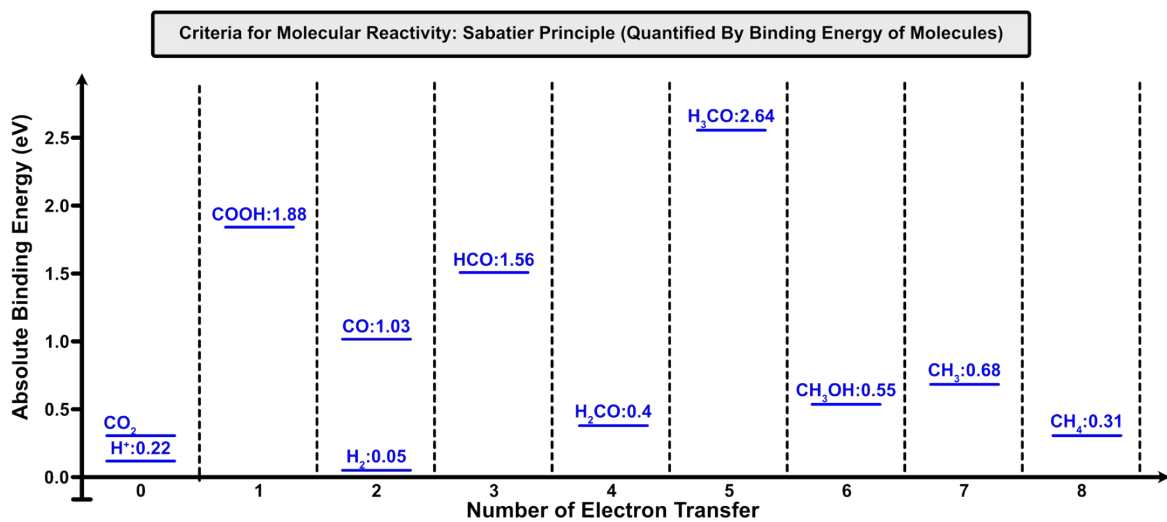
246

247 **Figure S5.** Binding energy of reagents, intermediates, and products in the reaction of CO_2RR

248 and HER.
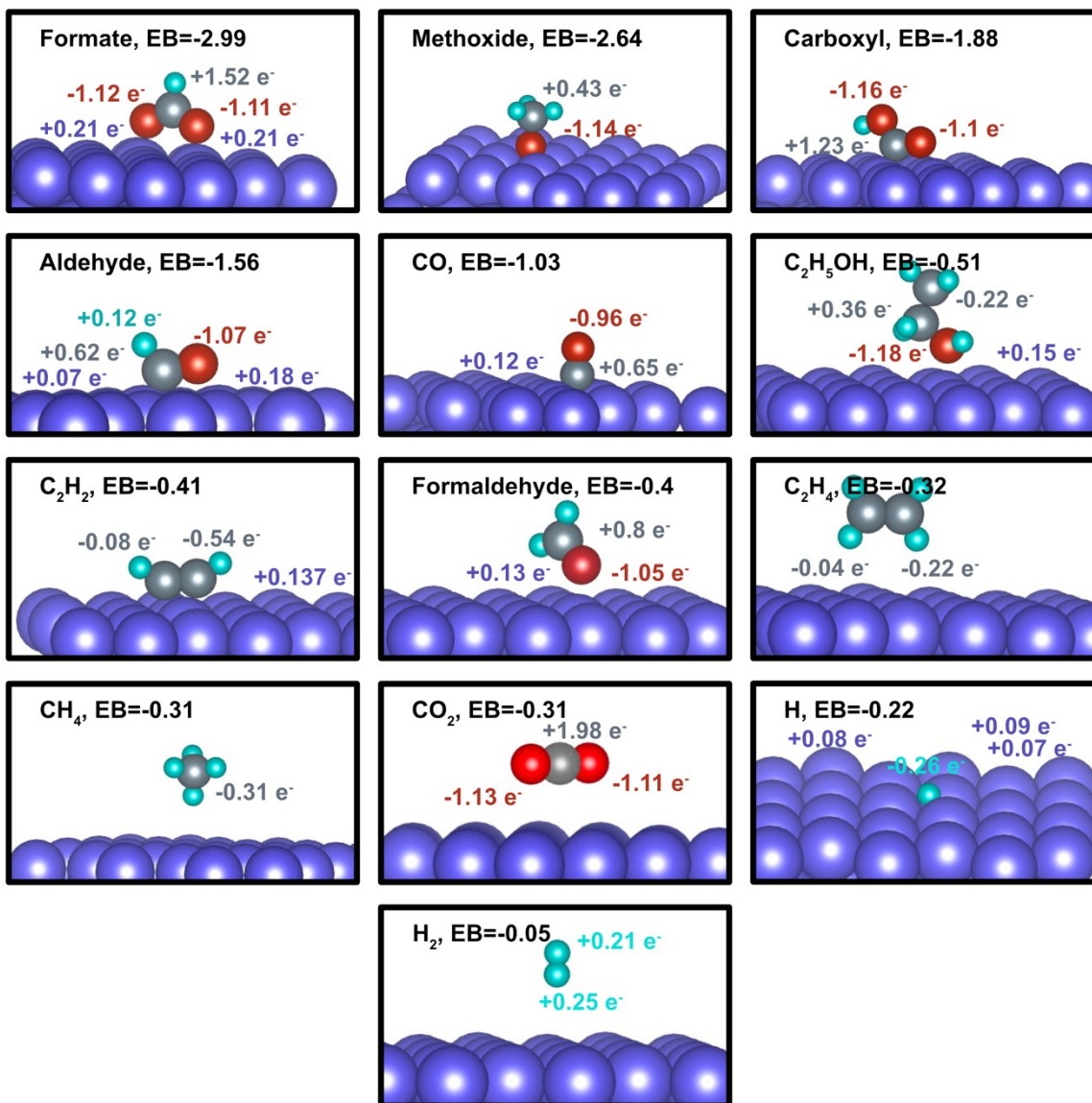
Figure S6. Bonding energy and bonding distances of major CO_2RR reactants, intermediates, and products. Units of EB is eV in these figures. The EB values of the mentioned species are in agreement with previously reported studies[32].

CO₂+H⁺+e⁻↔COOH⁻ (EA: 1.88 eV) — Barrier energy diagram with Energy difference [eV] on the y-axis and Reaction coordinate [Å] on the x-axis, showing the transition state configuration.
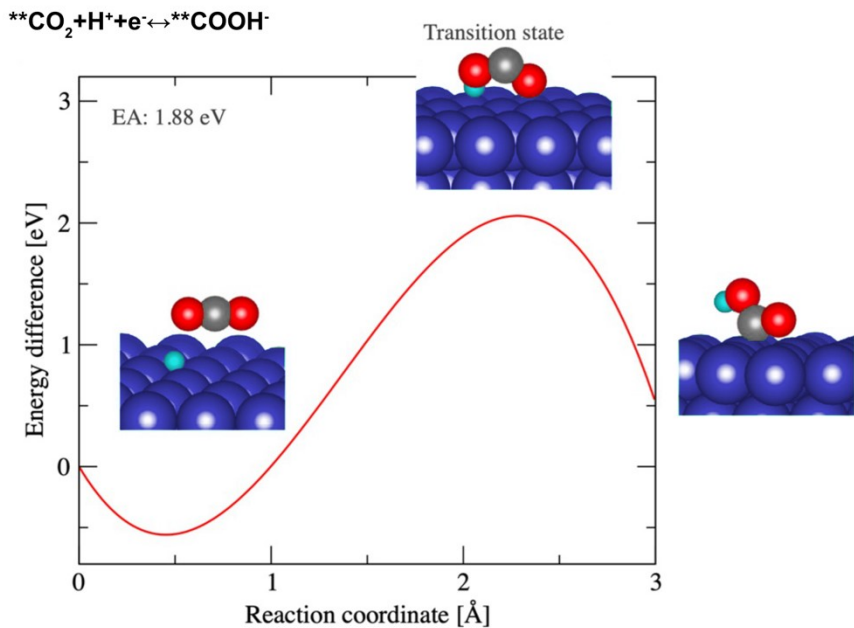
256

257 **Figure S7**. Barrier energy of CO_2 activation. This diagram shows the configuration of transition

258 states of activated CO_2 after the first proton-electron pair. It demonstrates the stable configuration

259 of the CO_2-Cu(111) characterized by the parallel adsorption of CO_2 onto the Cu surface. The

260 adsorption energy is found to be -0.31 eV indicating the physisorption nature of the CO_2 onto the

261 Cu surface in the beginning.

262

**COOH+e⁻↔*CO+*+OH⁻(aq)
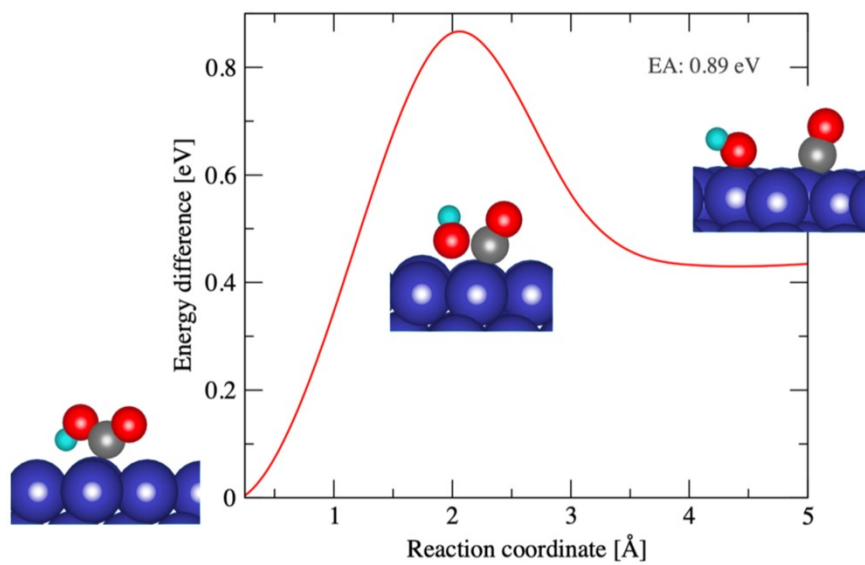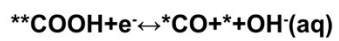
263

264 **Figure S8**. Barrier energy of CO generation. This diagram shows the process of dissociation of

265 the HO-CO bond.
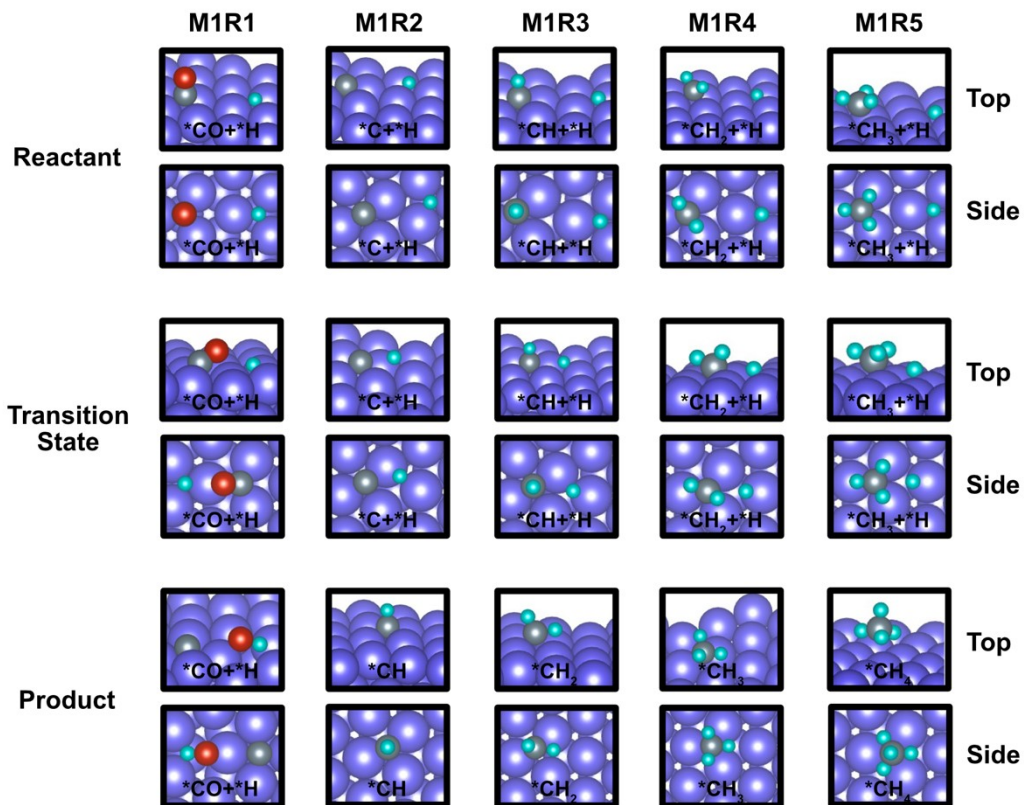
266
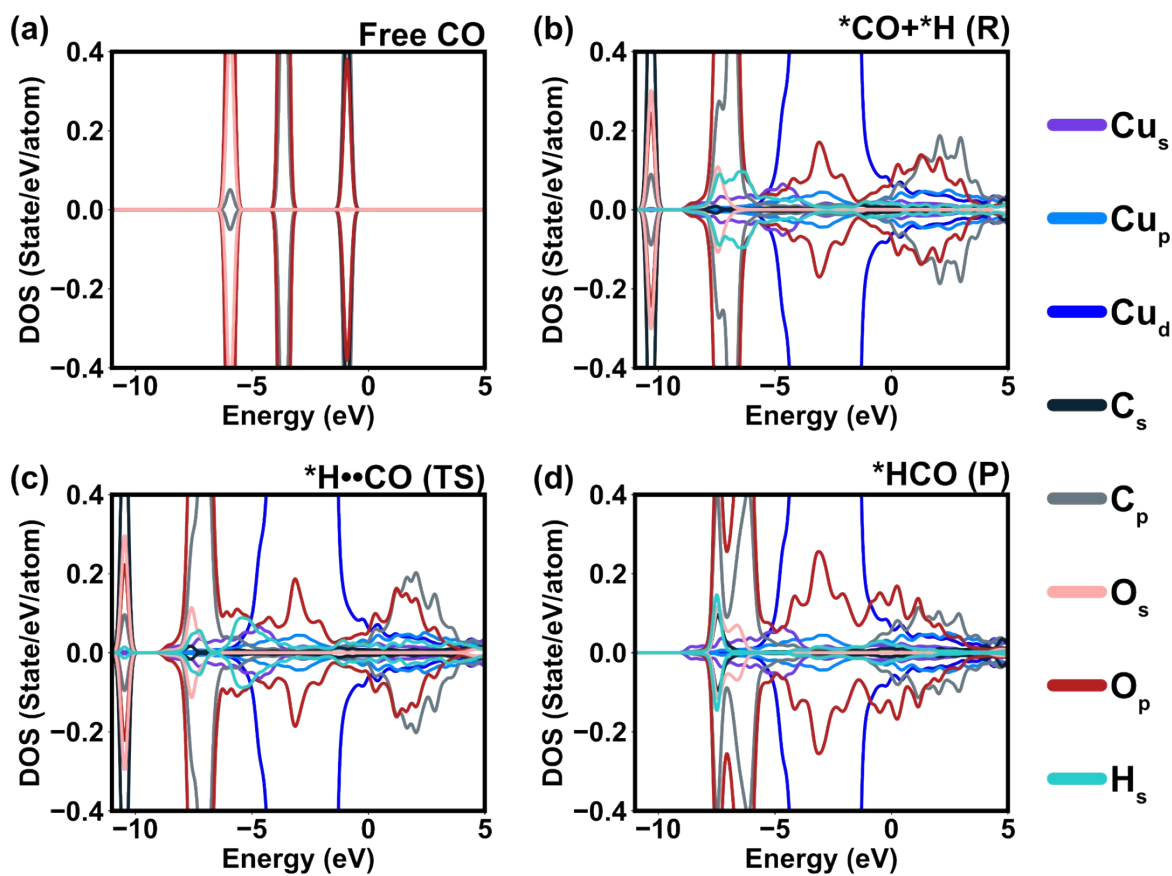
Figure S9. During CO protonation, the Density of state (DOS) results of (a) free CO, (b) *CO and *H as reactants, (c) transition state of *CO·· *H, and (d) final product of *HCO.
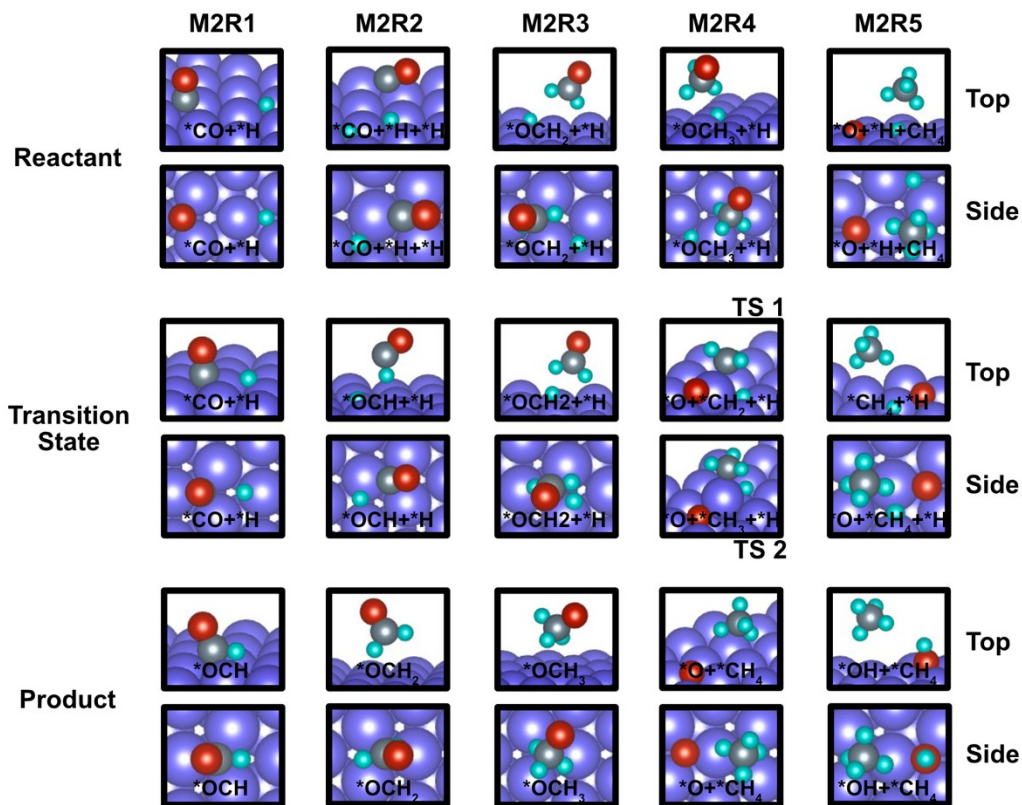
Figure S10. Configurations of reactants, transition states and products in Mechanism I. M1R1 represents "Mechanism I, reaction step 1", with the same for all others.
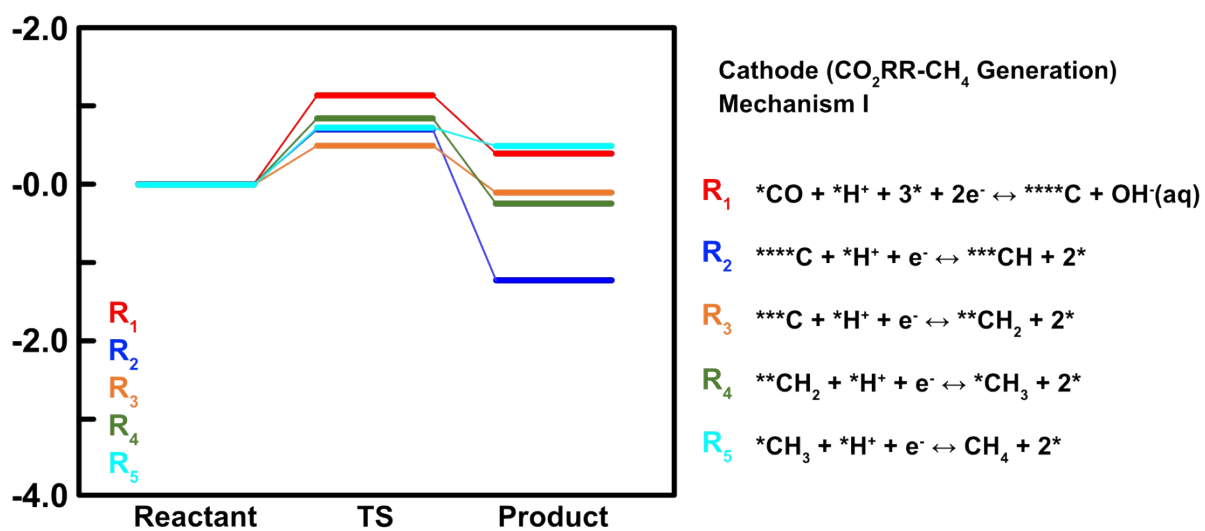
Figure S11. Configurations of reactants, transition states and products in Mechanism II. M2R1 represents "Mechanism II, reaction step 1", with the same for all others.

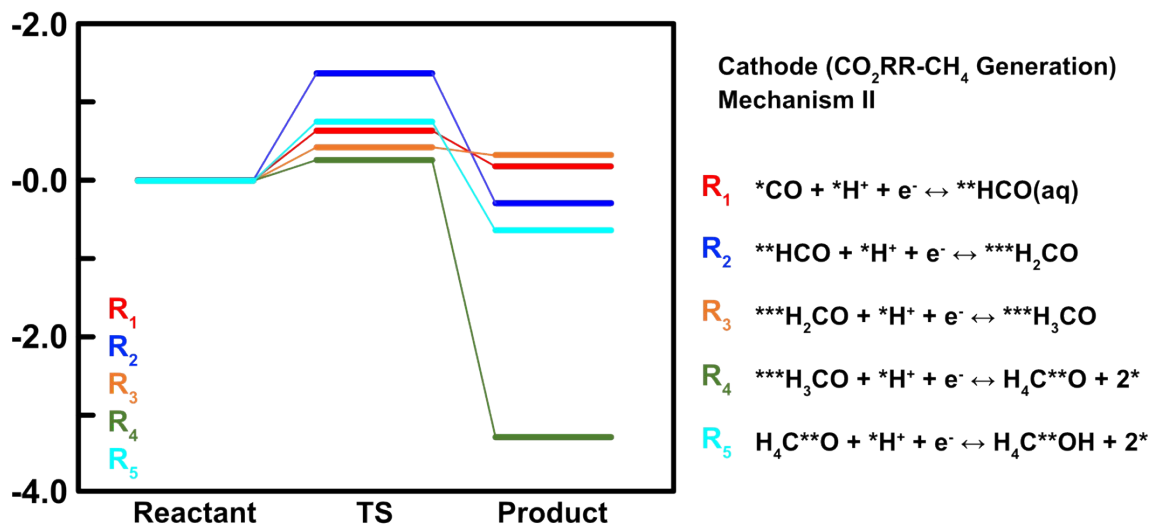Cathode (CO_2RR-CH_4 Generation)
Mechanism I

R_1 $*CO + *H^+ + 3* + 2e^- \leftrightarrow ****C + OH^-(aq)$

R_2 $****C + *H^+ + e^- \leftrightarrow ***CH + 2*$

R_3 $***C + *H^+ + e^- \leftrightarrow **CH_2 + 2*$

R_4 $**CH_2 + *H^+ + e^- \leftrightarrow *CH_3 + 2*$

R_5 $*CH_3 + *H^+ + e^- \leftrightarrow CH_4 + 2*$

281

Figure S12. Reaction pathways for the CO_2RR indicating the barrier energies of CO protonation

for CH_4 formation under Mechanism I. The color codes represent the reaction series happening

towards the CH_4 formation.

285

286

Cathode (CO_2RR-CH_4 Generation)
Mechanism II

R_1 *CO + *H$^+$ + e$^-$ ↔ **HCO(aq)

R_2 **HCO + *H$^+$ + e$^-$ ↔ ***H$_2$CO

R_3 ***H$_2$CO + *H$^+$ + e$^-$ ↔ ***H$_3$CO

R_4 ***H$_3$CO + *H$^+$ + e$^-$ ↔ H$_4$C**O + 2*

R_5 H$_4$C**O + *H$^+$ + e$^-$ ↔ H$_4$C**OH + 2*

287

Figure S13. Reaction pathways for the CO_2RR indicating the barrier energies of CO protonation

for CH_4 formation under Mechanism 2. The color codes represent the chain of reactions happening
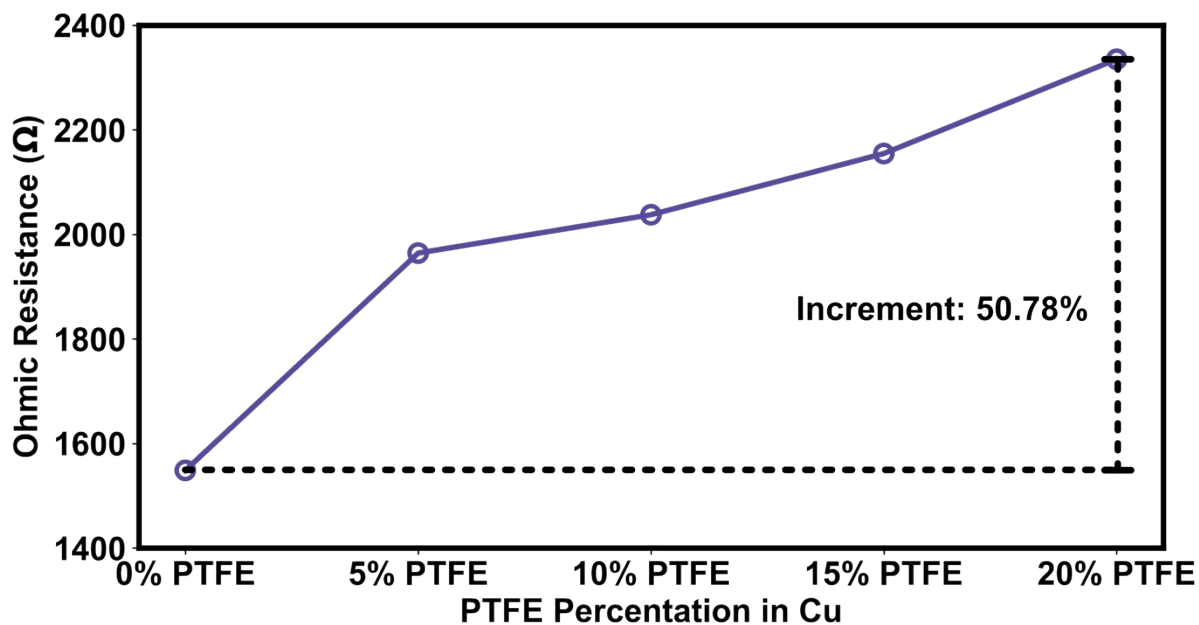
towards the CH_4 formation.

291

292

293
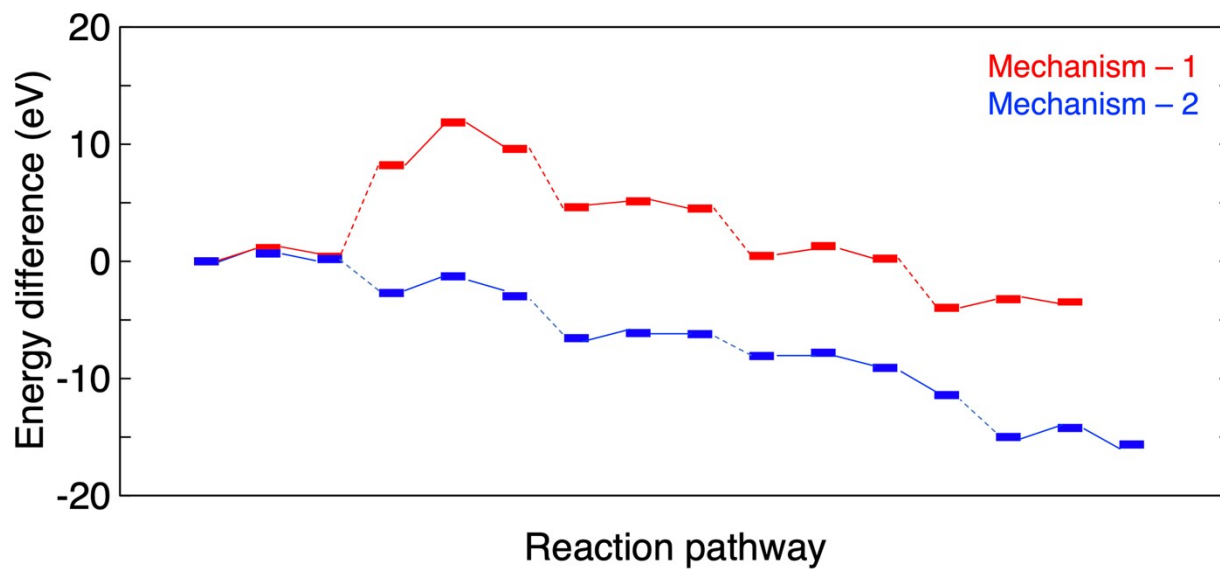
Figure S14. Complete energy profile comparison of CO_2RR towards CH_4 generation through
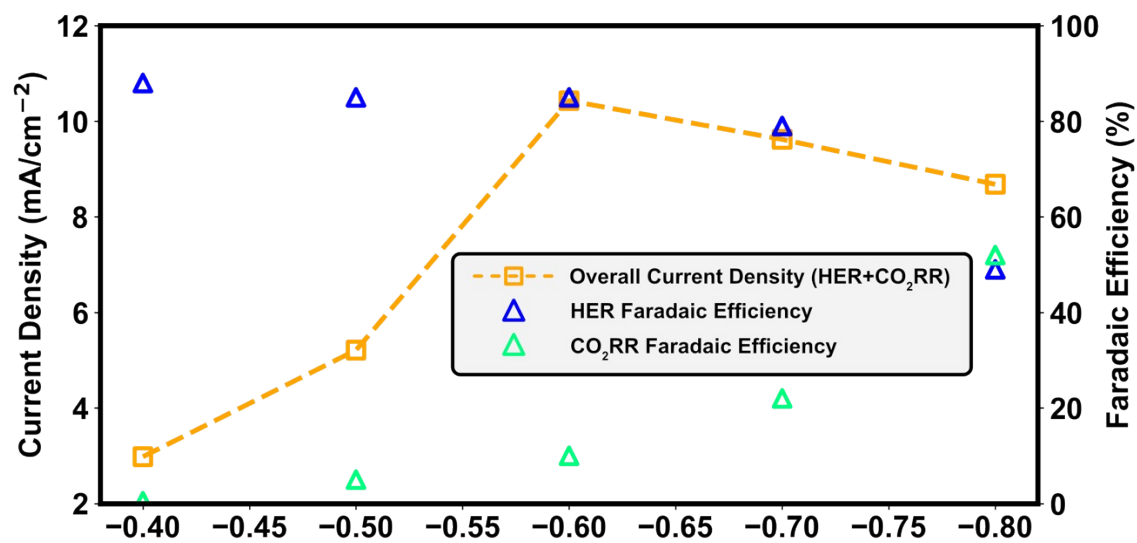
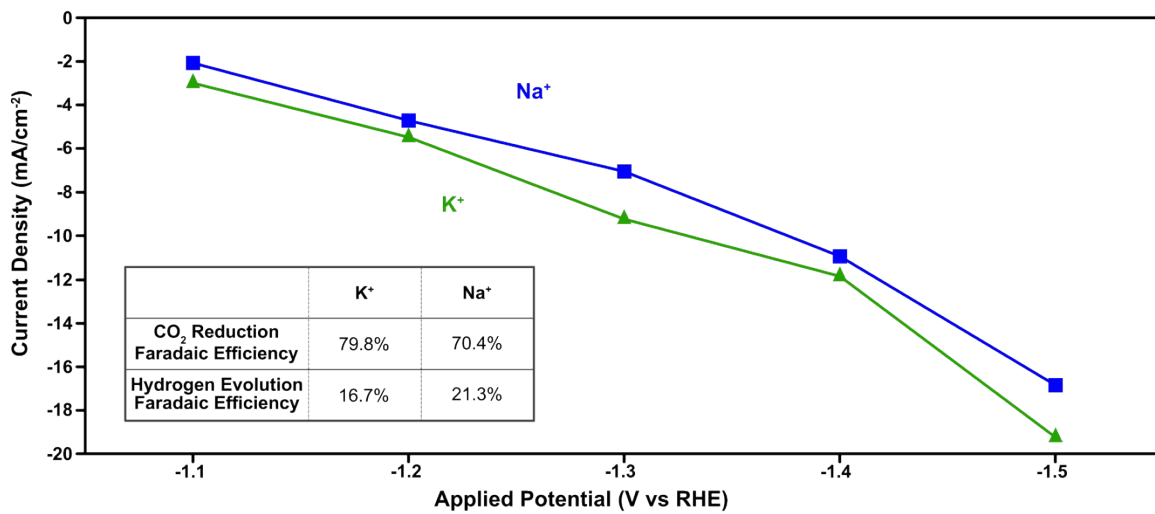295 Mechanisms I and II.

296

Increment: 50.78%

297

298   **Figure S15**. Ohmic resistance of the pristine Cu cathode and PTFE-Cu cathode at different PTFE

299   ratios from 0% to 20%.

300

301
302 **Figure S16**. Current density of overall system including HER and CO_2RR, and the Faradaic

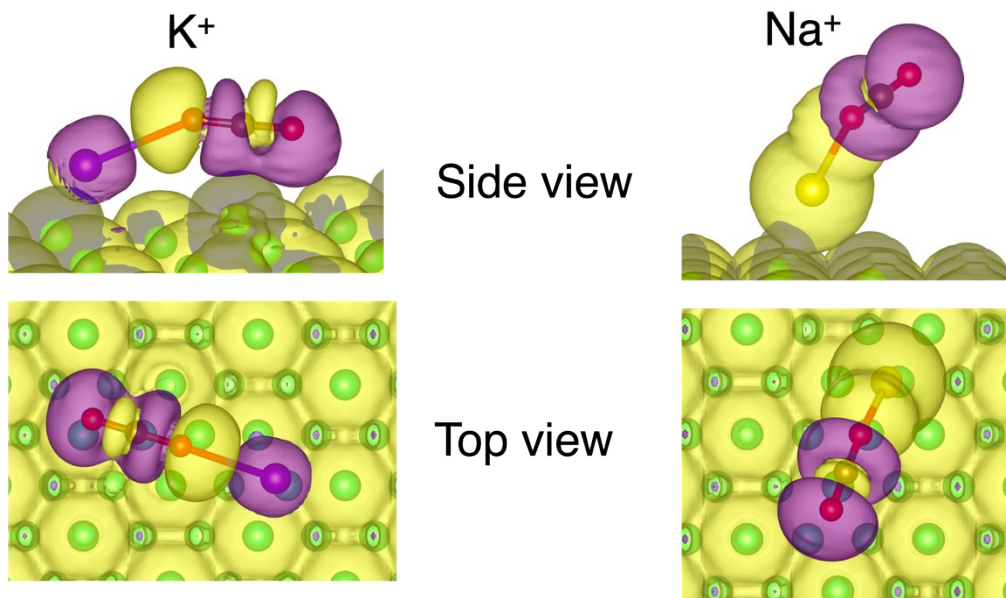303 efficiency (FE) of HER and CO_2RR, separately.

304

Figure S17. Difference of Faradaic efficiency (FE) and current density of the CO_2RR system with 0.1 M $KHCO_3$ (green line) and 0.1M $NaHCO_3$ (blue line).
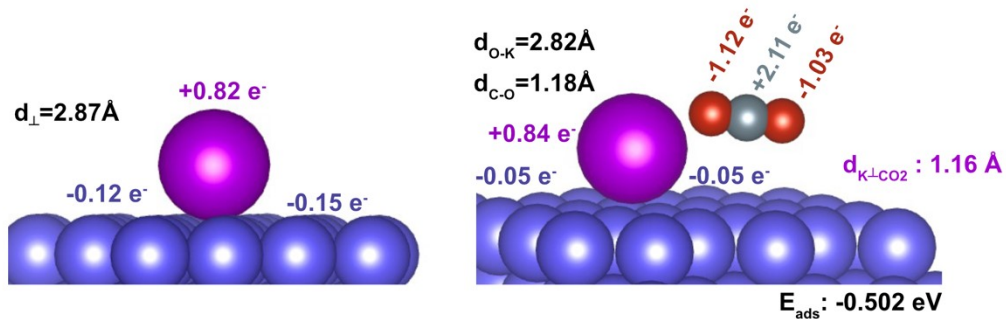
310

311 **Figure S18**. Side view and top view diagrams of electron cloud of K^+-CO_2 and Na^+-CO_2.

312

313

- Nearly parallel orientation of CO_2 on K-Cu(111) is highly preferred.
- CO_2 is located near potassium atom.
- Irregular stretching of C-O bond distances compared to that of the free CO_2 (dCO=1.16 Å).
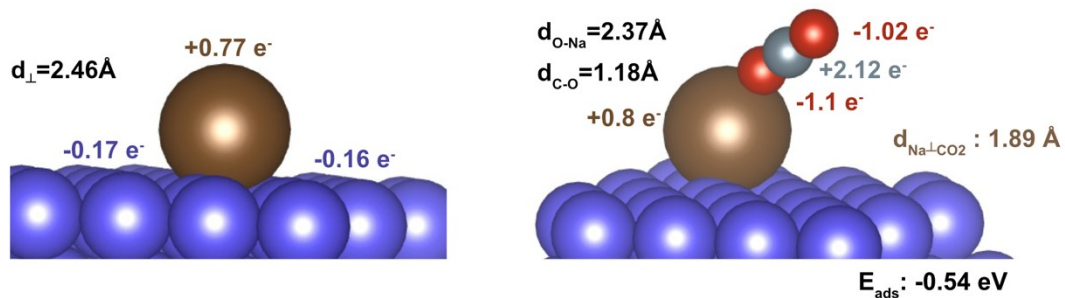- Presence of potassium ion enhances the BE of CO_2.

**Figure S19**. Configurations of K^+ on the Cu catalyst and its stabilization effect with absorbed CO_2 molecules.

- Tilted orientation of CO_2 on Na-Cu(111) is highly preferred.
- CO_2 adsorption onto the Na site takes place.
- Irregular stretching of C-O bond distances compared to that of the free CO_2 (dCO=1.16 Å).
- Presence of sodium leads to enhanced binding of CO_2.

319

320 **Figure S20**. Configurations of Na^+ on the Cu catalyst and its stabilization effect with absorbed

321 CO_2 molecules.
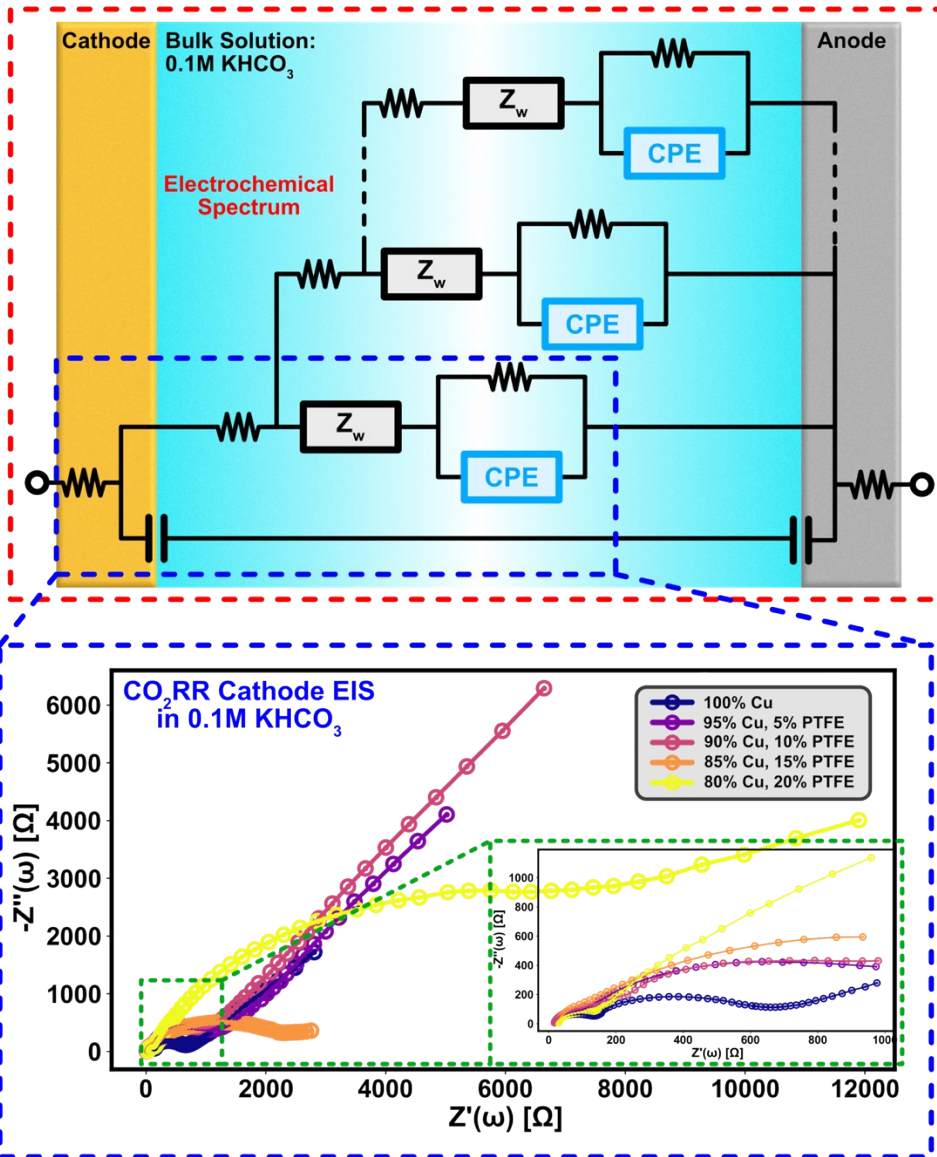
Figure S21. Simplified equivalent circuit of the CO$_2$RR system and the electrochemical impedance spectroscopy (EIS) experimental results of the pristine Cu and PTFE-Cu cathodes at different PTFE ratios from 0% to 20%.

330
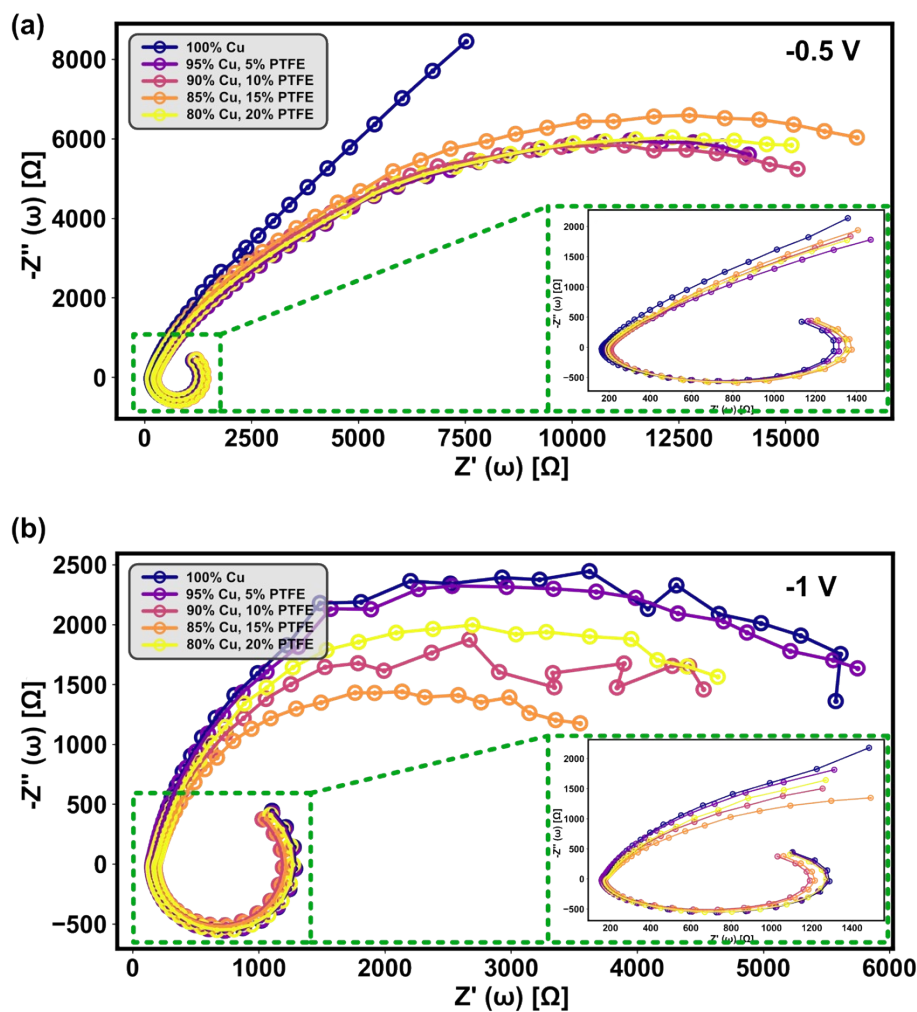
Figure S22. (a) EIS experimental results of H^+ diffusion across proton exchange membrane
(PEM) towards the pristine Cu and PTFE-Cu cathodes with the PTFE ratios from 5% to 20%
under -0.5V; (b) EIS experimental results of H^+ diffusion across PEM towards the pristine Cu
and PTFE-Cu cathodes with the PTFE ratios from 5% to 20% under -1V.

335
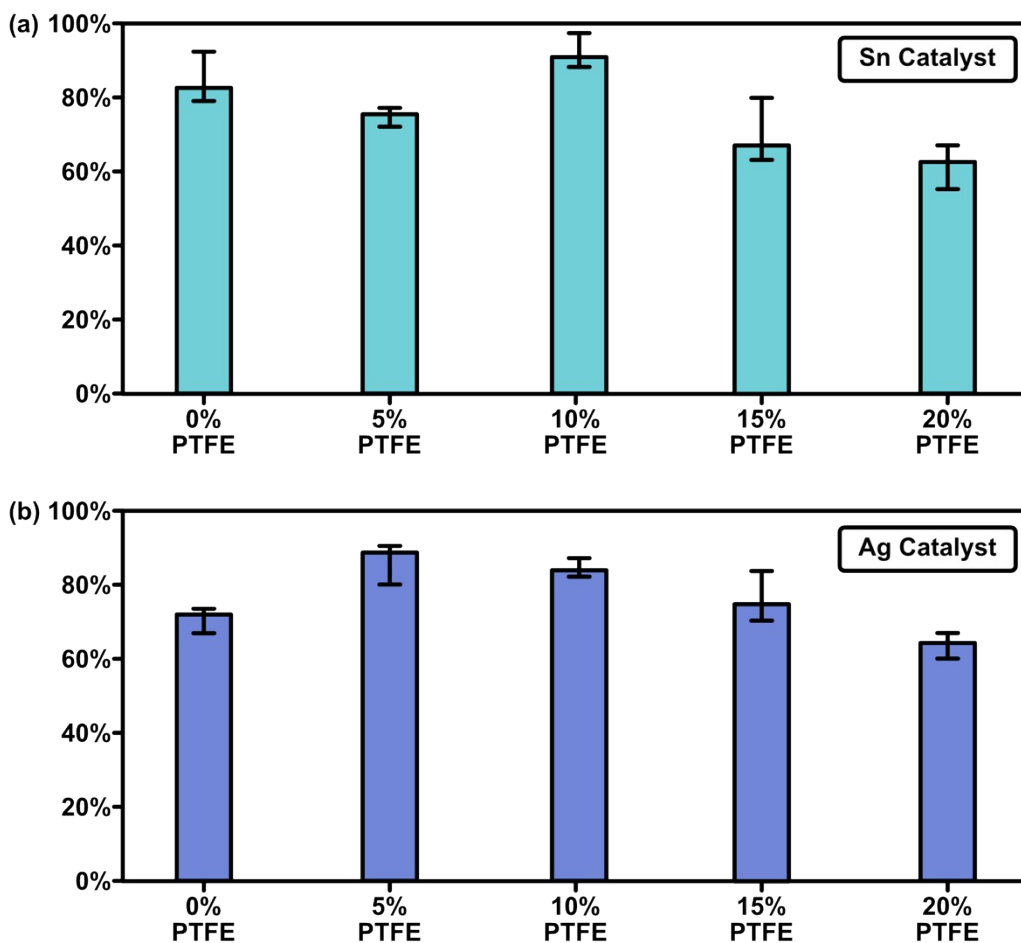
336

337 **Figure S23**. (a) The Faradaic efficiency (FE) of Sn catalyst with the PTFE ratios of 0%, 5%,

338 10%, 15%, and 20%; and (b) Faradaic efficiency (FE) of Ag catalyst with the PTFE ratios of 0%,

339 5%, 10%, 15%, and 20% under the external potential of -2.1V vs Ag/AgCl.

340
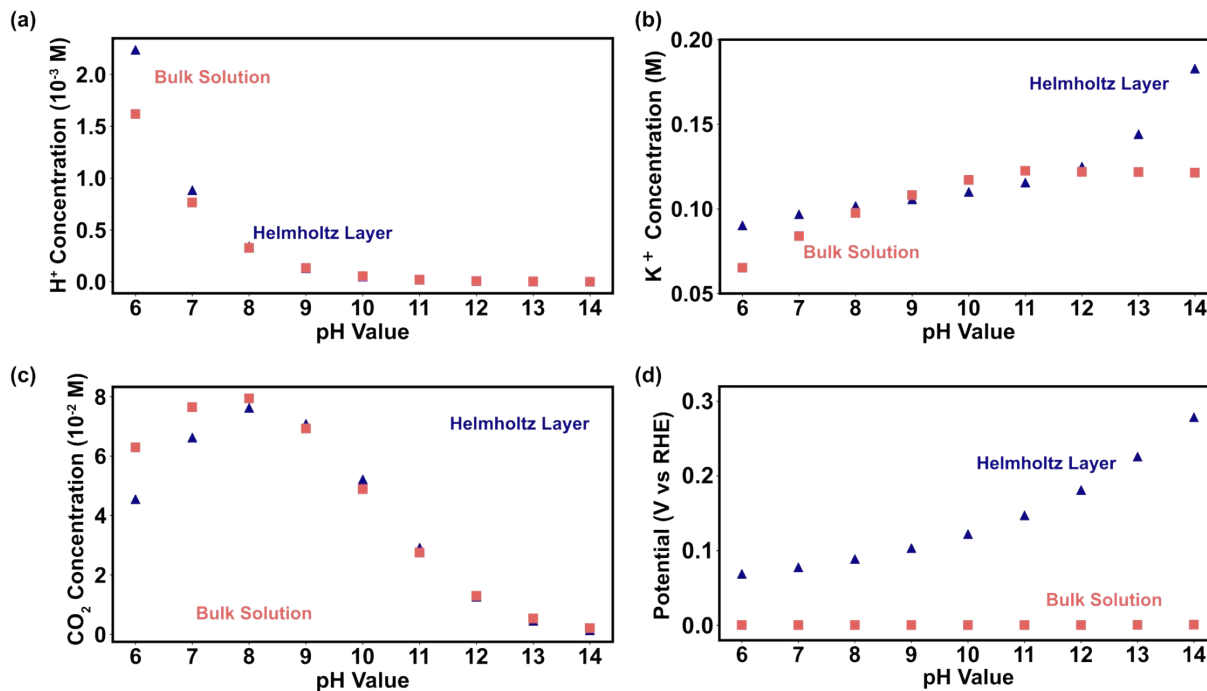
Figure S24. Variation of H^+, K^+, CO_2, and electrical potential in the Helmholtz layer and bulk solution under pH from 6 to 14. (a) Cathodic H^+ concentration in Helmholtz layer and bulk solution; (b) Cathodic K^+ concentration in Helmholtz layer and bulk solution; (c) Cathodic CO_2 concentration in Helmholtz layer and bulk solution; (d) Cathodic potential drop in Helmholtz layer and bulk solution.

346

347

348
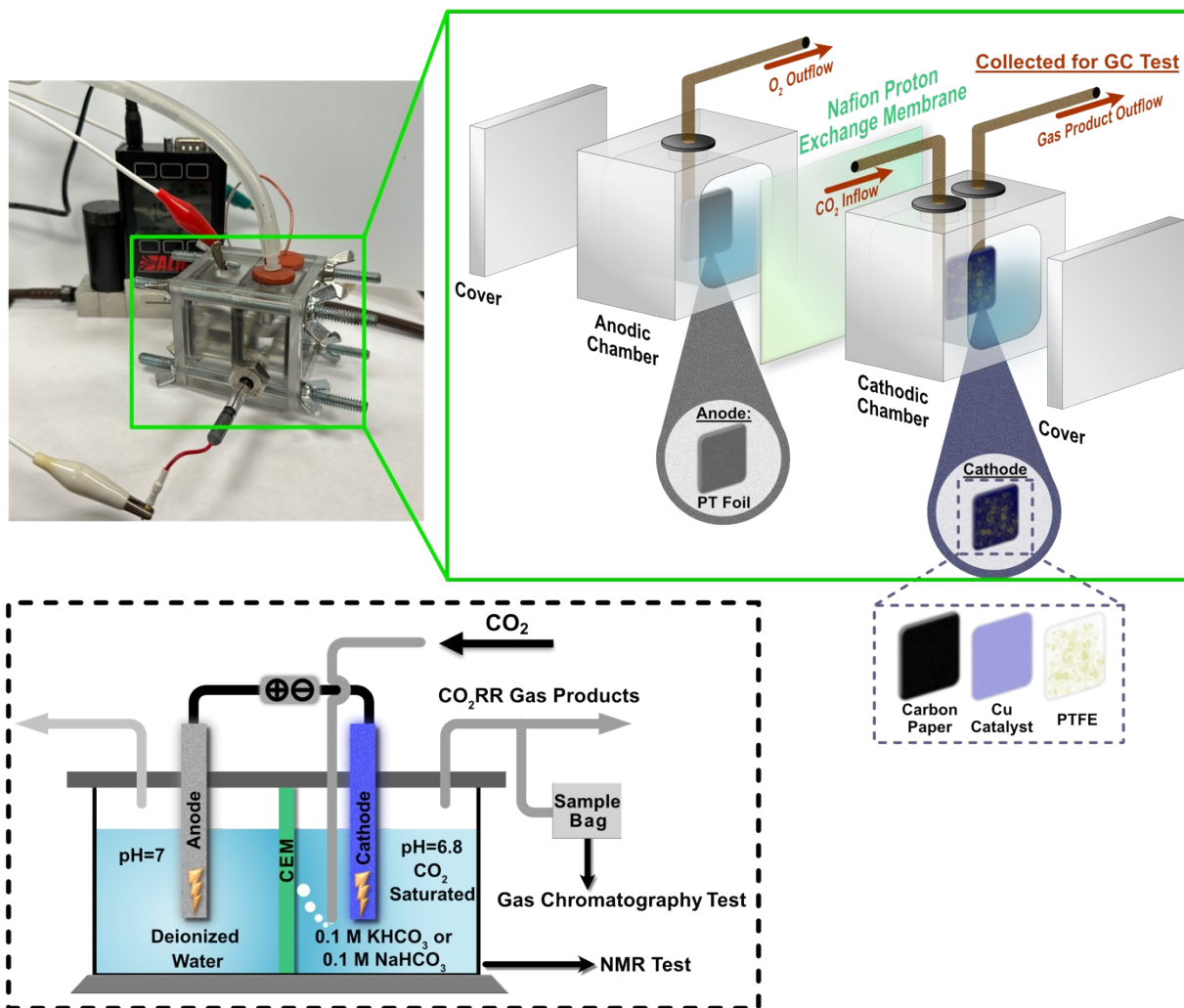
Figure S25: Diagram of the system setup for the CO_2RR experiments.

349

350

351
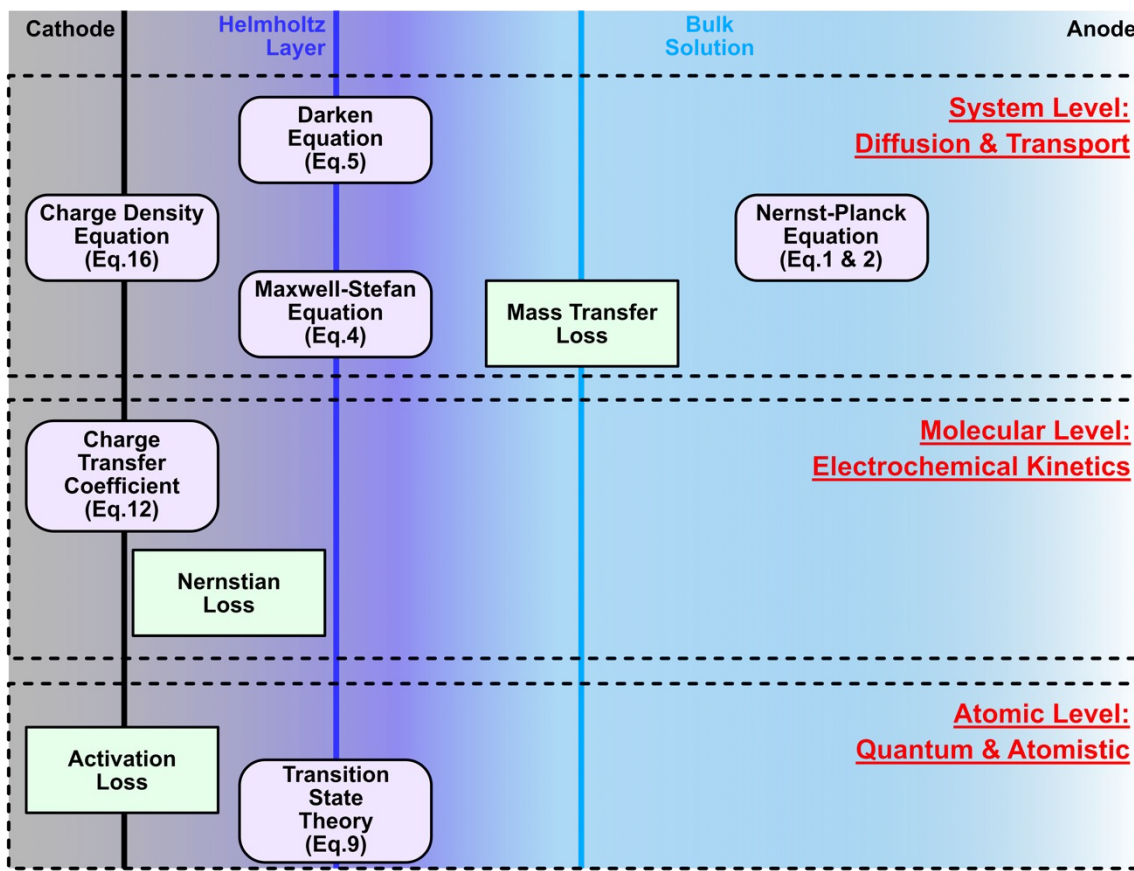
Figure S26. Governing equations at each layer of the multiscale model. The dash line box categorizes the equations according to the three levels of the multiscale model as is discussed in the main context. The vertical lines in different colors define the spatial location that each equation is applied in the CO_2RR system.

80%Cu 20% PTFE	85%Cu 15% PTFE	90%Cu 10% PTFE	95%Cu 5% PTFE	100%Cu 0% PTFE

359
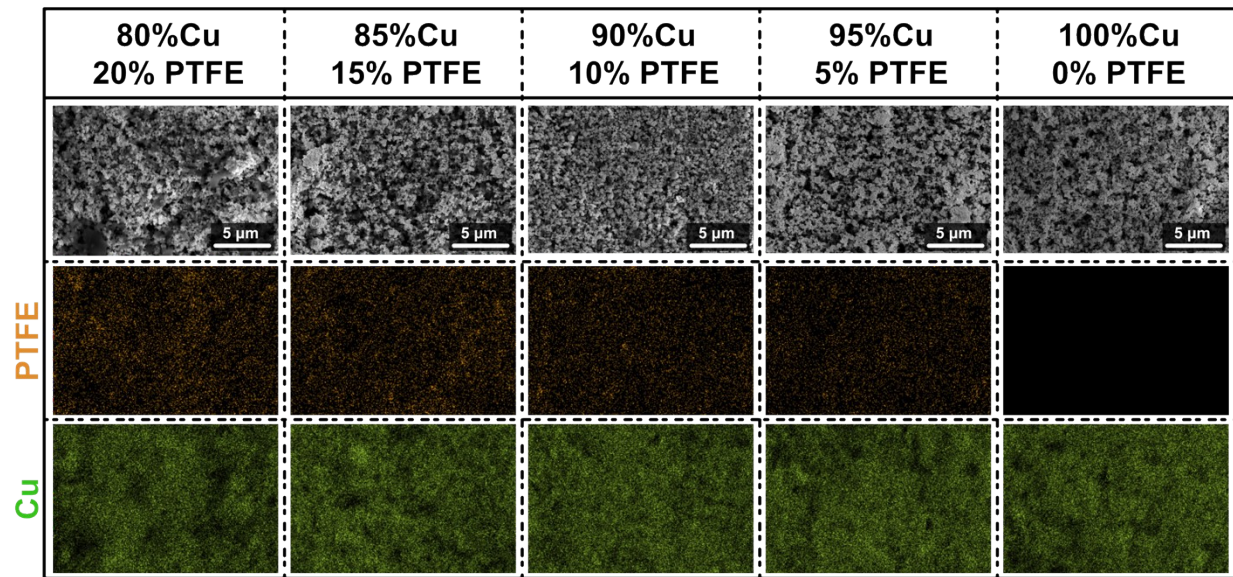
Figure S27. The corresponding SEM images of EDAX mappings in Figure 2b.

361

362 **Table S1.** Percentage of Cu and PTFE in the cathodes for experiment, as well as the original SEM

363 and EDAX mapping for each Cu-PTFE ratio

	Theoretical 80%Cu	*Theoretical 85%Cu*	*Theoretical 90%Cu*	*Theoretical 95%Cu*	*Theoretical 100%Cu*
Cu	81.86%	84.76%	89.55%	91.89%	100%
PTFE	18.14%	15.24%	10.45%	8.11%	0%

364

365

366 **Table S2**. Barrier energy and free energies of CO generation.

	Barrier Energy (eV)	Free Energy (eV)
R1	1.89	0.52
R2	0.87	0.44

367

368

369

370 **Table S3**. Barrier energies and free energies of CH$_4$ generation in Mechanism I.

	Barrier Energy (eV)	Free Energy (eV)
M1R1	1.14	0.4
M1R2	0.75	-1.24
M1R3	0.5	-0.12
M1R4	0.83	-0.23
M1R5	0.73	0.5

371

372

373

374 **Table S4**. Barrier energies and free energies of CH_4 generation in Mechanism II.

	Barrier Energy (eV)	Free Energy (eV)
M1S1	0.68	1.2
M2S2	1.42	0.17
M2S3	0.44	0.35
M2S4	0.28	-3.33
M2S5	0.77	0.64

375

376

377

378

379 **Table S5.** Bond length and distance of molecules between molecule and Cu atom (Unit: Å).

	d_{C-O}	d_{C-H}	$d_{\perp Cu}$	d_{O-H}	d_{C-C}	d_{H-H}
HCOO	1.27	1.11	1.99	/	/	/
CH$_3$O	1.44	1.1	1.37	/	/	/
COOH	1.3	/	2	0.98	/	/
CHO	1.25	1.12	1.9	/	/	/
CO	1.17	/	1.57	/	/	/
C$_2$H$_5$OH	1.45	1.1	2.27	0.97	1.52	/
C$_2$H$_2$	/	1.08	2.04	/	1.27	/
CH$_2$O	1.22	1.11	2.37	/	/	/
C$_2$H$_4$	/	1.09	3.24	/	1.33	/
CH$_4$	/	1.09	3.12	/	/	/
CO$_2$	1.18	/	3.51	/	/	/
H	/	/	0.98 (Note)	/	/	/
H$_2$	/	/	3.46	/	/	0.75

380

381 *Note:* The chemisorption bond length of Cu-H is 1.74 Å.

382

383 **Table S6**. T-tests of Faradaic efficiency (FE) results obtained for CH_4 and CO .

384 a. CH_4 FE t-statistics table:

	0%	5%	10%	15%	20%
0%	0	-0.113	-0.409	-0.073	-0.143
5%	-0.113	0	-0.294	0.04	-0.025
10%	-0.409	-0.294	0	0.333	0.28
15%	-0.073	0.04	0.333	0	-0.066
20%	-0.143	-0.025	0.28	-0.066	0

385

386 b.   CO FE t- statistics table:

	0%	5%	10%	15%	20%
0%	0	-0.704	0.097	0.276	1.246
5%	-0.704	0	0.666	0.776	1.541
10%	0.097	0.666	0	0.158	0.934
15%	0.276	0.776	0.158	0	0.711
20%	1.246	1.541	0.934	0.711	0

387

388 **Table S7**. Boundary condition of Nernst-Planck equation and Poisson equation.

	$c_{0,init}$ *(Variable)* *(mol/m³)*	$c_{\infty,Bulk}$ *(Constant)* *(mol/m³)*
CO_2	0	1.55×10^{-5}
H^+	1.1138	1.1138
OH^-	0.74659	0.74659
K^+	100	100
HCO_3^-	59.943	59.943
CO_3^{2-}	1.7584	1.7584

389

391 **Table S8**. Diffusion coefficients of molecules[33].

	Diffusion Coefficient $(10^{-9}\ m^2/s)$
CO_2	1.6
H^+	9.31
OH^-	5.27
K^+	1.96
Na^+	1.33
HCO_3^-	1.18
CO_3^{2-}	0.955

392

393
394 **Reference:**

1 Q. Zheng and G.-W. Wei, *J. Chem. Phys.*, 2011, **134**, 194101.

2 S. Hassani, in *Mathematical Methods: For Students of Physics and Related Fields*, ed. S. Hassani, Springer, New York, NY, 2009, pp. 139–170.

3 D. Bohra, J. H. Chaudhry, T. Burdyny, E. A. Pidko and W. A. Smith, *Energy Environ. Sci.*, 2019, **12**, 3380–3389.

4 T. Allie-Ebrahim, Q. Zhu, P. Bräuer, G. D. Moggridge and C. D'Agostino, *Phys. Chem. Chem. Phys.*, 2017, **19**, 16071–16077.

5 X. Liu, T. J. H. Vlugt and A. Bardow, *Ind. Eng. Chem. Res.*, 2011, **50**, 10350–10358.

6 B. Eren, R. S. Weatherup, N. Liakakos, G. A. Somorjai and M. Salmeron, *J. Am. Chem. Soc.*, 2016, **138**, 8207–8211.

7 Y.-H. Fang and Z.-P. Liu, *ACS Catal.*, 2014, **4**, 4364–4376.

8 V. I. Birss and A. Damjanovic, *J. Electrochem. Soc.*, 1983, **130**, 1694.

9 A. H. Motagamwala and J. A. Dumesic, *Chem. Rev.*, 2021, **121**, 1049–1076.

10 M. E. Björketun, V. Tripkovic, E. Skúlason and J. Rossmeisl, *Catal. Today*, 2013, **202**, 168–174.

11 N. D. Lang and W. Kohn, *Phys. Rev. B*, 1970, **1**, 4555–4568.

12 K. Besteman, M. A. G. Zevenbergen and S. G. Lemay, *Phys. Rev. E*, 2005, **72**, 061501.

13 B. E. Logan, E. Zikmund, W. Yang, R. Rossi, K.-Y. Kim, P. E. Saikaly and F. Zhang, *Environ. Sci. Technol.*, 2018, **52**, 8977–8985.

14 M. Arif, S. C. P. Cheung and J. Andrews, *Energy Fuels*, 2020, **34**, 13010–13022.

15 D. Yu and S. Yuvarajan, in *Nineteenth Annual IEEE Applied Power Electronics Conference and Exposition, 2004. APEC '04.*, 2004, vol. 1, pp. 362-366 Vol.1.

417   16 A. K. Sharma, K. Ahmed and E. Birgersson, *Ionics*, 2018, **24**, 2047–2054.

418   17 J. P. Perdew, K. Burke and M. Ernzerhof, *Phys. Rev. Lett.*, 1996, **77**, 3865–3868.

419   18 L. Vitos, A. V. Ruban, H. L. Skriver and J. Kollár, *Surf. Sci.*, 1998, **411**, 186–202.

420   19 G. Kresse and J. Furthmüller, *Comput. Mater. Sci.*, 1996, **6**, 15–50.

421   20 P. E. Blöchl, *Phys. Rev. B*, 1994, **50**, 17953–17979.

422   21 G. Henkelman, A. Arnaldsson and H. Jónsson, *Comput. Mater. Sci.*, 2006, **36**, 354–360.

423   22 J. K. Nørskov, J. Rossmeisl, A. Logadottir, L. Lindqvist, J. R. Kitchin, T. Bligaard and H.

424   Jónsson, *J. Phys. Chem. B*, 2004, **108**, 17886–17892.

425   23 J.-L. Liu and C.-L. Li, *AIP Adv.*, 2019, **9**, 015214.

426   24 R. R. Netz, *Phys. Rev. E*, 1999, **60**, 3174–3182.

427   25 M. Huš, D. Kopač, N. S. Štefančič, D. L. Jurković, V. D. B. C. Dasireddy and B. Likozar,

428   *Catal. Sci. Technol.*, 2017, **7**, 5900–5913.

429   26 A. Pavlišič, M. Huš, A. Prašnikar and B. Likozar, *J. Clean. Prod.*, 2020, **275**, 122958.

430   27 A. Alhajaj and N. Shah, *Int. J. Greenh. Gas Control*, 2020, **94**, 102925.

431   28 A. Alhajaj, N. M. Dowell and N. Shah, *Energy Procedia*, 2013, **37**, 2552–2561.

432   29 M. I. Alam, R. Cheula, G. Moroni, L. Nardi and M. Maestri, *Catal. Sci. Technol.*, 2021, **11**,

433   6601–6629.

434   30 Q. Sun and Z. Liu, *Front. Chem. China*, 2011, **6**, 164.

435   31 M. R. Singh, J. D. Goodpaster, A. Z. Weber, M. Head-Gordon and A. T. Bell, *Proc. Natl.*

436   *Acad. Sci.*, 2017, **114**, E8812–E8821.

437   32 L. Xu, J. Lin, Y. Bai and M. Mavrikakis, *Top. Catal.*, 2018, **61**, 736–750.

438   33 Table of Diffusion Coefficients, https://www.aqion.de/site/diffusion-coefficients, (accessed

439   May 17, 2023).

440